# Numerical modelling of 3D plastic flow and heat transfer during friction stir welding of stainless steel

**R. Nandan[1], G. G. Roy[1], T. J. Lienert[2] and T. DebRoy[1]***

Three-dimensional (3D) viscoplastic flow and temperature field during friction stir welding (FSW) of 304 austenitic stainless steel were mathematically modelled. The equations of conservation of mass, momentum and energy were solved in three dimensions using spatially variable thermophysical properties using a methodology adapted from well established previous work in fusion welding. Non-Newtonian viscosity for the metal flow was calculated considering strain rate and temperature dependent flow stress. The computed profiles of strain rate and viscosity were examined in light of the existing literature on thermomechanical processing of alloys. The computed results showed significant viscoplastic flow near the tool surface, and convective transport of heat was found to be an important mechanism of heat transfer. The computed temperature and velocity fields demonstrated strongly 3D nature of the transport of heat and mass indicating the need for 3D calculations. The computed temperature profiles agreed well with the corresponding experimentally measured values. The non-Newtonian viscosity for FSW of stainless steel was found to be of the same order of magnitude as that for the FSW of aluminium. Like FSW of aluminium, the viscosity was found to be a strong function of both strain rate and temperature, while strain rate was found to be the most dominant factor. A small region of recirculating plasticised material was found to be present near the tool pin. The size of this region was larger near the shoulder and smaller further away from it. Streamlines around the pin were influenced by the presence of the rotating shoulder, especially at higher elevations. Stream lines indicated that material was transported mainly around the pin in the retreating side.

**Keywords:** Friction stir welding, Plastic flow, Heat transfer, Viscosity, Stainless steel

## Introduction

Friction stir welding (FSW) is a solid state welding process in which the base metal does not melt during the process. During FSW, a rotating tool moves along the joint interface, generates heat and results in recirculating flow of plasticised material near the tool surface. The tool usually has a large diameter shoulder and a smaller threaded pin. A schematic diagram of the FSW system is shown in Fig. 1. Heat generated at and near the interface between the tool and the work piece is transported into the workpiece and the tool. In addition, the properties of the metal change depending on the temperature and the strain rate. The motion of the plasticised metal depends on both the material properties and the welding variables such as the rotational and the translational speeds of the tool and the tool design. The rotational and the translational speeds determine the local values of the relative velocities between the tool and the workpiece. As a result, the local heat generation rates differ between the advancing and the retreating sides of the workpiece, as shown in Fig. 1*b*. The complex interactions between the various simultaneously occurring physical processes affect the heating and cooling rates and the structure and properties of the welded joints.

Unlike the fusion welding processes, the FSW process is relatively new. Since its inception in 1991 at TWI,[1] FSW has been widely examined both experimentally and theoretically for better understanding of the welding process as well as the welded materials. Most of the early quantitative studies were based on heat conduction, and they ignored the plastic flow near the tool.[2,3] Schmidt *et al.*[4] proposed a general analytical model for heat generation based on the nature of the contact at the tool matrix interface namely sliding, sticking or partial sticking conditions. Based on the experimental data on heat generation they concluded that the sticking condition prevailed at the tool/matrix interface of 2024-T3

[1]Department of Materials Science and Engineering, The Pennsylvania State University, University Park, PA 16802, USA
[2]Materials Science and Technology Division, Los Alamos National Laboratory, Los Alamos, NM, USA

*Corresponding author, email debroy@psu.edu


Published by Maney on behalf of the Institute
Received 6 February 2006; accepted 11 March 2006
DOI 10.1179/174329306X107692

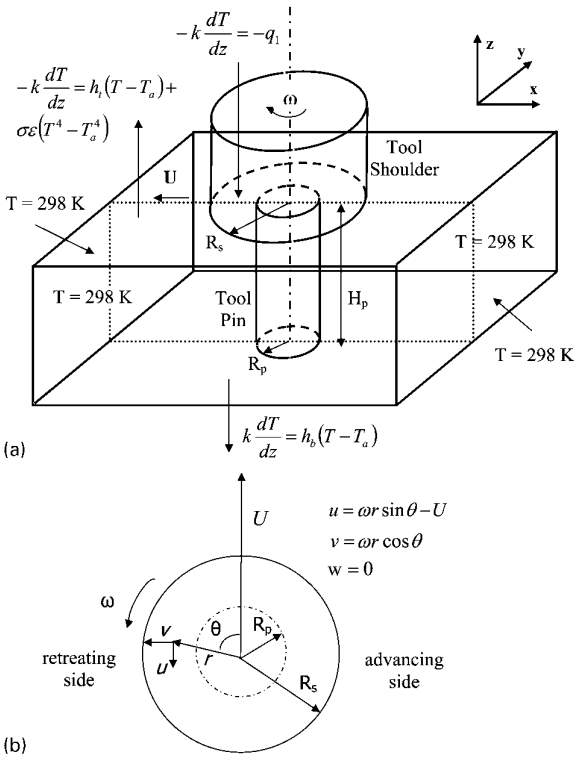


**1** ***a*** **schematic diagram of FSW system considered in model showing thermal boundary conditions and** ***b*** **top view of tool showing velocity boundary conditions at tool surface**

aluminium alloy. Friggard *et al.*[5] assumed that frictional heating at the tool shoulder/workpiece interface was entirely responsible for the heat generation during welding. The anticipated reduction of friction at the interface at elevated temperatures owing to localised plasticity was considered by adjusting the coefficient of friction at elevated temperatures to prevent melting. Chao *et al.*[6] estimated the fraction of the heat generated at the tool shoulder interface that is transported into the workpiece during FSW of aluminium alloy based on overall heat balance both in the tool and in the workpiece using inverse modelling. Their calculations showed that only 5% of the heat generated at the interface was transported into the tool. Song and Kovacevic[7] developed a transient three-dimensional (3D) thermal model for both the tool and the workpiece during FSW of 6061Al alloy. They estimated the partitioning of heat at the tool/workpiece interface by an iterative numerical method. Computed temperatures from their model agreed well with the experimental measurements. Khandkar *et al.*[8] developed a 3D thermal model where the heat generation was modelled based on experimentally measured torque distribution. However, they adjusted the heat transfer coefficient at the bottom of the workpiece to achieve good agreement between the computed and the measured temperatures. Although the heat conduction models provided important insight about the FSW process, these initial models ignored convective heat transfer owing to viscoplastic flow of metals.

Work on the development of rigorous models of heat transfer in FSW considering materials flow is just beginning. Seidel and Reynolds[9] developed a two-dimensional (2D) fully coupled thermal model based on laminar, viscous and non-Newtonian flow around a circular cylinder. The streamlines predicted from their model indicated that material transport occurs mainly around the pin in the retreating side. A plug of material near the tool was also observed owing to no slip condition at the wall. They observed that significant vertical mixing occurred during FSW, particularly at low values of welding speed to rotational speed ratios from their experimental tracer study.[10] This fact indicates the need for 3D models.

Colegrove and Shercliff[11,12] used a commercial CFD software, FLUENT, to develop a 3D heat and material flow model during FSW of 7075 Al alloy. They designed a tool, called Trivex, which is nearly triangular in shape with convex surfaces, and MX-Trivex which has the similar shape but with threads in it. They observed that although there was a marginal decrease in traversing force in the MX-Trivex tool from the Trivex tool, the traversing and downward forces were both considerably lower compared with that required for the conventional Triflute tool. Interestingly, the different tool designs did not result in any significant changes in either the heat input or the power requirement. In another study[13] they observed that traversing force required for tool raked at 2·5° from the direction of travel was lower than that of the tool normal to the workpiece. The decrease was attributed to favourable pressure redistribution behind the tool. The model predictions overestimated the deformation zone, peak temperature and underestimated the traversing force. They suggested that these discrepancies might be eliminated by considering slip at the tool/workpiece interface or drastically reducing the viscosity near the solidus temperature.

Smith *et al.*[14] experimentally determined viscosity as a function of shear rate and temperature for the AA 6061-T6 alloy, which was then incorporated into a 3D coupled thermal model for the FSW of 6061 aluminium alloy. They found that the viscous heat dissipation within the weld was a major source of heat generation. Furthermore, the frictional heating did not significantly contribute to the heat generation. Ulysse[15] modelled the effects of tool speeds, both rotational and linear, on forces and plate temperatures during FSW of thick aluminium plates, based on a 3D viscoplastic model. The modelling results indicated that the forces acting on the pin increased with increasing welding speeds and decreasing rotational speeds. The computed temperatures were found to be higher than the measured values and the discrepancy was attributed to inadequate representation of the constitutive behaviour of the metal for the wide range of strain rates, strains and temperatures typically encountered during the FSW process. Computed velocity fields or the order of magnitude of the velocities were not included in the paper.

Most recently, Nandan *et al.*[16] reported results of a 3D material flow and heat transfer modelling results during FSW of 6061 aluminium alloy. They calculated the temperature fields, cooling rates, plastic flow fields and the geometry of the thermomechanically affected zone (TMAZ), using spatially variable heat generation rates, non-Newtonian viscosity as a function of local strain rate and temperature, and temperature dependent thermal conductivity, specific heat and yield stress. The

computed temperature fields and TMAZ agreed well with the corresponding independent experimental data.

Although several numerical models of FSW of aluminium alloy have been reported in the literature, most of these were not concerned with the FSW of steel. There are few exceptions. Zhu and Chao[17] made a 3D thermal model without considering plastic flow for 304L stainless steel. They calculated the partitioning of heat at the shoulder/workpiece interface through inverse analysis based on experimentally measured temperature at selected monitoring locations. They[17] observed that $\sim$50% of the total mechanical energy was transported into the workpiece during the FSW of stainless steel. This is in contrast with the FSW of aluminium, where 75–80% of the mechanical energy flows into the workpiece.[6] The peak temperatures calculated from the model were reported in the 900–1000°C range. Two dimensional steady state heat transfer and fluid flow near the tool pin was modelled by Cho *et al.*[18] for the FSW of stainless steel. They used simplified Hart's model[19] to calculate the flow stress and non-Newtonian viscosity. Isotropic strain hardening was included in the finite element solution procedure. The workpiece temperatures were computed assuming various tool temperatures and heat transfer coefficients. As expected, they found that higher tool temperatures and higher heat transfer coefficients resulted in higher workpiece temperatures. The experimental and the computed results indicated that the temperatures were $\sim$100 K higher on the advancing side than on the retreating side.

The above discussion indicates that significant progress has been made in the numerical simulation of the FSW process, particularly for aluminium. A few studies have also been reported on the quantitative understanding of FSW of steels. However, a detailed numerical simulation involving 3D material flow coupled with heat transfer during FSW of austenitic stainless steel has not been reported. Here, the authors present a detailed numerical analysis of 3D material flow and heat transfer during FSW of stainless steel. In particular, the authors examine the temperature fields, cooling rates, the plastic flow fields by solving the equations of conservation of mass, momentum and energy in three dimensions with appropriate boundary conditions. The computed values of strain rates, viscosity, velocities and temperatures during FSW of austenitic stainless steel are compared with the corresponding values typically obtained during the FSW of aluminium alloys. The nature of materials flow around the pin is examined through the examination of streamlines. The model considers spatially variable heat generation rates, non-Newtonian viscosity as a function of local strain rate, temperature and the nature of the material, and temperature dependent thermal conductivity, specific heat and yield stress. Numerically computed temperature fields were compared with the corresponding experimentally measured values.

## Mathematical modelling

### Assumptions

Except at the beginning and end of welding, heat is generated at a constant rate during the intermediate period and the cross-sections of the welds demonstrate similar geometry, structure and properties indicating a quasi-steady behaviour. Shortly after the start of welding, the cylindrical tool shoulder and the tool pin rotate at a constant speed with the tool pin completely inserted within the workpiece. The mass flow is treated as a flow of a non-Newtonian, incompressible, visco-plastic material. The maximum shear stress for yielding was assumed to be $\tau = \sigma_{\text{yield}}/3^{1/2}$ where the yield stress $\sigma_{\text{yield}}$ is based on distortion energy theory for plane stress. The density variation was ignored following Boussinesq's approximation. Partial sticking condition was assumed at the surface between the tool and the workpiece.

### Governing equations

The continuity equation for incompressible single phase flow in index notation for $i$=1, 2, 3, representing $x$, $y$ and $z$ directions respectively is given by

$$\frac{\partial u_{\text{i}}}{\partial x_{\text{i}}} = 0 \tag{1}$$

where $u$ is the velocity of plastic flow. The steady single phase momentum conservation equations with reference to a co-ordinate system attached to the heat source in index form may be represented as[20]

$$\rho \frac{\partial u_{\text{i}} u_{\text{j}}}{\partial x_{\text{i}}} = -\frac{\partial P}{\partial x_{\text{j}}} + \frac{\partial}{\partial x_{\text{i}}}\left(\mu \frac{\partial u_{\text{j}}}{\partial x_{\text{i}}} + \mu \frac{\partial u_{\text{i}}}{\partial x_{\text{j}}}\right) - \rho U \frac{\partial u_{\text{j}}}{\partial x_{\text{j}}} \tag{2}$$

where $\rho$ is the density and $\mu$ is the non-Newtonian viscosity and $U$ is the welding velocity, $P$ is the pressure. The viscosity was calculated based on simplified Hart's model,[19] where the flow stress $\sigma_{\text{e}}$ is expressed as the summation of two contributions, plastic contribution $\sigma_{\text{P}}$ and viscous contribution $\sigma_{\text{V}}$

$$\sigma_{\text{e}} = \sigma_{\text{P}} + \sigma_{\text{V}} \tag{3}$$

the viscous contribution represents the frictional force along the slip plane that resist the dislocation glide. The plastic contribution represents the flow resistance from dislocation entanglement. The flow stress owing to plastic contribution $\sigma_{\text{P}}$ and viscous contribution $\sigma_{\text{V}}$ are expressed as

$$\sigma_{\text{P}} = \kappa \exp\left[-\left(\frac{b}{\dot{\varepsilon}}\right)^{\lambda}\right] \tag{4}$$

where,

$$b = b_0 \left(\frac{\kappa}{G}\right)^{\text{N}} \exp\left(-\frac{Q}{RT}\right) \tag{5}$$

and

$$\sigma_{\text{V}} = G\left(\frac{\dot{\varepsilon}}{a}\right)^{1/\text{M}} \tag{6}$$

where,

$$a = a_0 \exp\left(-\frac{Q^0}{RT}\right) \tag{7}$$

$\dot{\varepsilon}$ is the deformation rate, $R$ is the universal gas constant, $T$ is the absolute temperature. $G$, $Q$, $Q^0$, $a_0$, $b_0$, $\lambda$, $N$, $M$ are material parameters which are determined from experiments and are given in Table 1. The plastic contribution is represented by a scalar state variable $\kappa$, which may be considered as the density and strength of barriers to the motion of dislocations through the crystal

**Table 1 Material parameters for simplified Hart's model for 304 stainless steel[18]**

| Parameter | Value |
|---|---|
| $a_0$, $s^{-1}$ | $1{\cdot}36 \times 10^{35}$ |
| $b_0$, $s^{-1}$ | $8{\cdot}03 \times 10^{26}$ |
| $G$, GPa | 73·1 |
| $\kappa_0$, MPa | 150·0 |
| $Q$, kcal $mol^{-1}$ | 98 |
| $Q^0$, kcal $mol^{-1}$ | 21·7 |
| $\lambda$ | 0·15 |
| $M$ | 7·8 |
| $N$ | 5·0 |
| $C$, MPa | 2·148 |
| $D_0$, $s^{-1}$ | $1{\cdot}0 \times 10^{8}$ |
| $m_0$ | 2·148 |
| $n_0$ | 6 |

structure. It may be observed from equation (4) that $\kappa$ represents the upper limit of $\sigma_P$. In FSW, where the deformation rate is high, it is reasonable to use an evolution equation for $\kappa$ which specifies a saturation value of strength $\kappa_s$ as a function of temperature and deformation rate. However, for simplicity, in the present calculation, strain hardening has not been considered and a saturation value for $\kappa$ has been used, which can be expressed as[18]

$$k_s = \left(\frac{C}{\varphi}\right)^{m_0} \tag{8}$$

where, $\phi$, the Fisher factor is given as[21]

$$\varphi = T \ln\left(\frac{D_0}{\dot{\varepsilon}}\right) \tag{9}$$

the experimentally determined material parameters, $D_0$, $C$, $m_0$ are given in Table 1.

Finally, viscosity can be determined from flow stress and effective strain rate using Perzyna's viscoplasticity model[22]

$$\mu = \frac{\sigma_e}{3\dot{\varepsilon}} \tag{10}$$

where $\dot{\varepsilon}$ is the effective strain rate and is given by

$$\dot{\varepsilon} = \left(\frac{2}{3}\varepsilon_{ij}\varepsilon_{ij}\right)^{\frac{1}{2}} \tag{11}$$

where $\varepsilon_{ij}$ is the strain rate tensor, defined as

$$\varepsilon_{ij} = \frac{1}{2}\left(\frac{\partial u_i}{\partial x_j} + \frac{\partial u_j}{\partial x_i}\right) \tag{12}$$

figure 2 shows the computed variation of viscosity, expressed as logarithm to the base of ten, with strain rate and temperature. The results show that viscosity decreases significantly with both strain rate and temperature. The strain rate is the most dominant factor for the conditions typical of FSW.

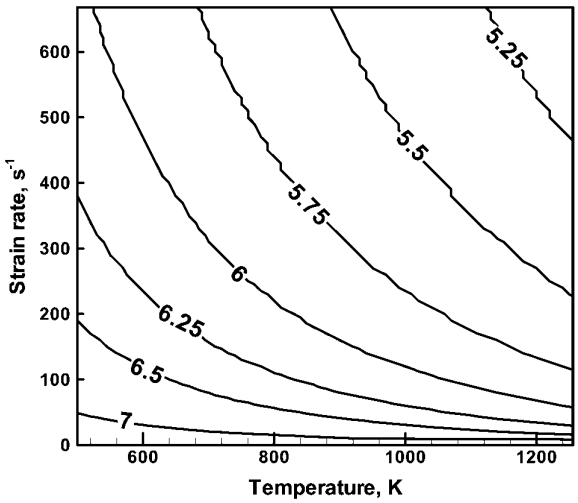


**2 Computed contours of viscosity as function of temperature and strain rate: viscosity in kg $m^{-1}$ $s^{-1}$ is expressed as logarithm to the base 10**

The computed values of viscosity for the FSW of stainless steel are roughly of the same order of magnitude as that for the welding of 6061 aluminium alloy[16] for the same strain rate and temperature combination. It should be noted that the viscosities near the tool/workpiece interface affect the torque requirement for welding. The temperatures near the tool/material interface are somewhat higher for the FSW of stainless steel than for the FSW of aluminium alloys. Considering this difference in temperature, the same order of magnitude of the viscosities of stainless steel and 6061 aluminium alloy near the tool/workpiece interface indicate that the torques may not be generally much higher for the welding of stainless steel than that for aluminium. The torque values depend on the welding variables, tool design and other factors such as the nature of the workpiece. In Table 2 the data reported in the literature show that the order of magnitude of the torque for the FSW of stainless steel was roughly of the same order of magnitude as that for the welding of aluminium alloys 6061 and 2024.

The steady thermal energy conservation equation is given by

$$\rho C_p \frac{\partial (u_i T)}{\partial x_i} = -\rho C_p U \frac{\partial T}{\partial x_i} + \frac{\partial}{\partial x_i}\left(k \frac{\partial T}{\partial x_i}\right) + [S(\theta) A_r / V] \tag{13}$$

where $\rho$ is the density, $C_p$ is the specific heat and $k$ is the thermal conductivity of the weld material. The term $S(\theta)$ represents the heat generation rate per unit area at the tool pin/workpiece interface, $A_r$ is any arbitrarily

**Table 2 Reported torque values for FSW of aluminium alloys and stainless steel**

| Material | Shoulder diameter, mm | Pin diameter, mm | Rotational speed, rev $min^{-1}$ | Welding speed, mm $s^{-1}$ | Average torque, N m | Reference |
|---|---|---|---|---|---|---|
| AA2024-T3 | 18·0 | 6·0 | 400 | 2·0 | 41·9 | 4 |
| AA6061-T651 | 25·4 | 10·0 | 390 | 2·36 | 73·4 | 8 |
| 304 stainless steel | 19·05 | 6·35 | 300 | 1·69 | 56·0 | 17 |
| 304 stainless steel | 19·05 | 6·35 | 500 | 1·69 | 42·8 | 17 |

selected area on the tool pin and $V$ is the volume over which the heat generated on $A_r$ is dissipated. The heat source, $S(\theta)$ for vertical surface of the tool pin may be defined as

$$S(\theta) = C_f \tau(\omega R_P - U \sin\theta) \quad (14)$$

similarly, $S(\theta)$ for the horizontal bottom surface of the tool pin is given by

$$S(\theta) = C_f \tau(\omega r - U \sin\theta) \quad (15)$$

where, $C_f$ is the power efficiency factor, i.e. the amount of mechanical energy converted to heat energy, the angular velocity $\omega$ is given by $2\pi N$, where $N$ is the number of revolution per second, $R_P$ is the tool pin radius. The velocity $(\omega r - U \sin\theta)$ represents the relative velocity of the tool with respect to the material. The variation of yield stress for 304 stainless steel alloy with temperature is shown in Fig. 3 based on data available in Ref. 23. The symbol $\theta$ represents the angle between a horizontal direction vector from the tool axis to any point on the cylindrical surface and the welding direction and may be defined in the Cartesian co-ordinate system as

$$\theta = \sin^{-1}\left[\frac{y}{\sqrt{(x^2+y^2)}}\right], \text{ or } \theta = \cos^{-1}\left[\frac{x}{\sqrt{(x^2+y^2)}}\right] \quad (16)$$

where (0,0) corresponds to the tool axis. Because the thermal conductivity of the tool material (tungsten) is $\sim$4 times higher than steel, a significant amount of heat will be transported to the tool material. Therefore, the total heat generated at the shoulder interface has been partitioned using the following analytical expression based on one-dimensional heat transfer[24]

$$\frac{J_W}{J_T} = \frac{\sqrt{(k\rho C_P)_W}}{\sqrt{(k\rho C_P)_T}} \quad (17)$$

where, $J$, $k$, $C_P$ and $\rho$ represent heat flux, thermal conductivity, specific heat and density of the material respectively. The subscript $W$ and $T$ represent the workpiece and tool respectively. Based on the data used in the present study at 1000 K, the estimated heat flux to the workpiece is calculated as 39%. This relation has been examined experimentally by Lienert *et al.*[25] and found to be suitable. Because of the simplifying nature of equation (17) the sensitivity of this ratio on peak temperature has been assessed, and the results will be discussed in the following section. The effect of strain rate on the yield stress has been discussed in the appendix. It is shown that in the range of strain rates encountered in the FSW of stainless steel, the strain rate sensitivity of yield stress can be ignored.

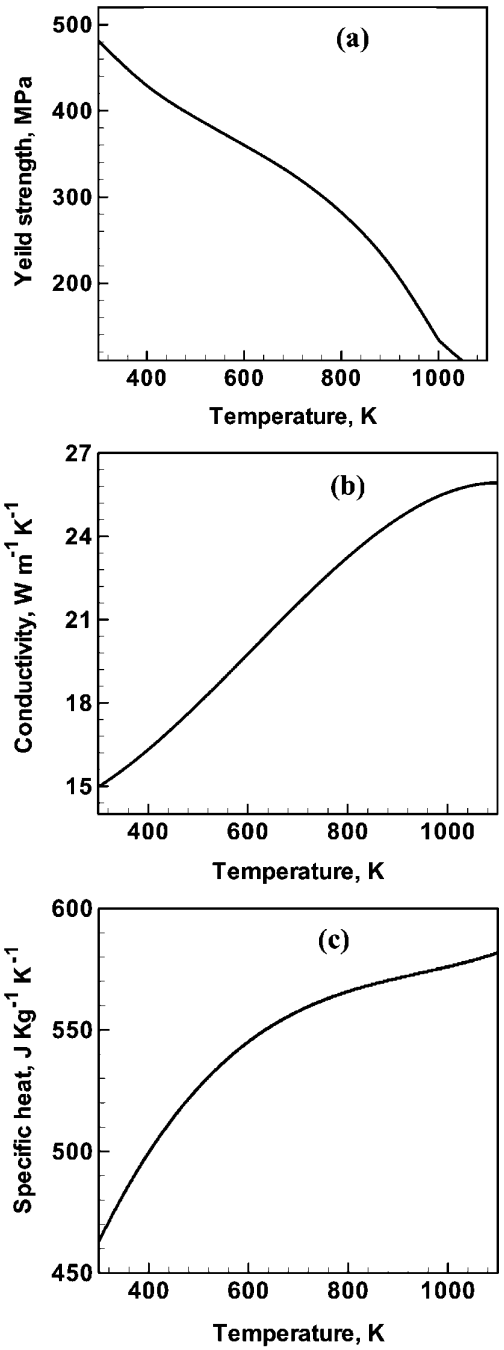


**3 Variations of *a* yield strength,[23] *b* thermal conductivity[23] and *c* specific heat capacity[23] of 304 stainless steel with temperature: symbols denote data points from literature while curves are obtained by spline interpolation of data points**

## Boundary conditions

A heat flux continuity at the shoulder/workpiece interface yields

$$k\left.\frac{\partial T}{\partial z}\right|_{top} = q_1 \quad \text{in the range } R_P \leqslant r \leqslant R_S \quad (18)$$

$R_P$ and $R_S$ represent the tool pin and shoulder radius respectively, and $q_1$ represents the rate of heat generation owing to plastic work at the shoulder/workpiece interface. It is given by

$$q_1 = C_f[\delta\tau(\omega r - U\sin\theta) + (1-\delta)\mu P_T]$$
$$= C_f\left[\delta\tau\left(\omega\sqrt{(x^2+y^2)} - U\sin\theta\right) + (1-\delta)\mu P_T\right] \quad (19)$$

where $\delta$ is the extent of sticking and $P_T$ is the applied pressure (plunge) on the shoulder. When $\delta$ is 1, full sticking is indicated and all the heat is generated by plastic deformation. When $\delta$=0, heat is generated only

**Table 3 Data used in calculations**

| Property/weld parameter | Value |
|---|---|
| Workpiece length (*x* direction), m | 0·30 |
| Workpiece width (*y* direction), m | 0·15 |
| Shoulder radius, mm | 9·53 |
| Pin radius, mm | 3·17 |
| Pin length, mm | 3·18 |
| Tool speed, mm $s^{-1}$ | 0·85–2·55 |
| Rotational speed, rev $min^{-1}$ | 300–500 |
| Workpiece material | 304 stainless steel |
| Density, kg $m^{-3}$ | 7200 |
| Solidus temperature,[32] K | 1697 |
| Plunge pressure[17] $P_T$, MPa | 109 |
| Coefficient of friction | 0·4 |
| Percentage sticking $\delta$ | 0·7 |
| Coefficient of thermal expansion,[32] $K^{-1}$ | $1{\cdot}96 \times 10^{-5}$ |
| Heat transfer coefficient from bottom,[34] W $m^{-2}$ $K^{-1}$ | 125 |
| Tool material | Tungsten |

by friction. The boundary condition for heat exchange between the top surface of the workpiece and the surroundings beyond the shoulder involved consideration of both convective and radiative heat transfer as

$$-k\left.\frac{\partial T}{\partial z}\right|_{\text{top}} = \sigma\varepsilon\left(T^4 - T_a^4\right) + h_c(T - T_a) \tag{20}$$

at the bottom surface, condition of Newtonian cooling under natural convection has been applied

$$k\left.\frac{\partial T}{\partial z}\right|_{\text{bottom}} = h(T - T_a) \tag{21}$$

velocity at the tool pin periphery have been defined in terms of tool translation velocity and the tool pin angular velocity

$$\begin{aligned} u &= \omega R_P \sin\theta - U \\ v &= \omega R_P \cos\theta \end{aligned} \tag{22}$$

similarly, at the shoulder contact, velocity condition may be written as

$$\left.\begin{aligned} u &= \omega r \sin\theta - U \\ v &= \omega r \cos\theta \end{aligned}\right\} \text{ in the range } R_p \leqslant r \leqslant R_s \tag{23}$$

at all other surfaces, temperatures are set at ambient temperature and the velocities are set to zero.

The governing equations and the boundary conditions were implemented in a computer code. The discretisation of the governing equations, implementation of the boundary conditions and the convergence and accuracy of the solutions are described in appendix A. The SIMPLE algorithm[26] based solution procedure, capable of calculating 3D heat transfer and fluid flow with a stationary or moving heat source, with a free or flat surface, has been well tested and has been recently reported for the calculations of heat transfer and fluid flow in several welding processes.[20,27–33] The data used for the calculations are presented in Tables 1 and 3.

## Results and discussion

### Heat generation rates

The proportion of the heat generated at the tool shoulder and the pin surface is determined by the tool geometry and the welding variables. For the experimental conditions studied in this work, the computed heat generation rates at the shoulder and the pin surface are presented in Table 4. The results show that for the welding conditions examined, $\sim$80% heat is generated at the shoulder, and 20% at the pin vertical surface. Previous work[17] has shown that $\sim$50% of the mechanical work is converted to heat during FSW of stainless steel. Therefore, the power input for various welding conditions can be approximately estimated by multiplying the heat generation rates given in Table 4 by two. The results show that the power input increases with rotational speed at a constant welding speed. Higher power input is also needed at higher welding speed at a constant rotational speed. Figure 4*a* and *b* shows the spatial variation of heat generation pattern at the tool/workpiece interfaces. Figure 4*a* shows that the heat generation pattern at the tool shoulder is nearly symmetric about the tool axis. The relative velocity between the workpiece and the shoulder increases with distance from the axis. As a result, more heat is generated further away from the axis near the shoulder. The angular variation of heat generation rate on the tool surface is shown in Fig. 4*b*. The non-uniformity in the heat generation pattern results from the difference in the relative velocity at different angular locations on the pin surface, which arises owing to the variation in term $U\sin\theta$. The local differences in heat generation rates lead to significant variations of local temperatures. Strong recirculation of a layer of plasticised material near the pin surface does not eliminate the difference. The flow pattern of the plasticised material and its role in heat transfer will be discussed later in the paper.

### Computed temperature fields

The computed temperature profiles along the longitudinal and transverse sections through tool axis and at the top surface of the workpiece are shown in Fig. 5*a–c* respectively. The temperature profiles on the longitudinal midsection (Fig. 5*a*) and on the top surface of

**Table 4 Heat generated at various surfaces of tool as function of rotational and translational speed**

| Weld speed, mm $s^{-1}$ | Rotational speed, rev $min^{-1}$ | Heat input from shoulder, W | Heat input from tool pin, W | Maximum temperature, K |
|---|---|---|---|---|
| 0·85 | 300 | 496 | 63 | 1316 |
| 1·70 | 300 | 602 | 91 | 1241 |
| 2·55 | 300 | 705 | 113 | 1200 |
| 0·85 | 400 | 558 | 54 | 1412 |
| 1·70 | 400 | 668 | 88 | 1313 |
| 2·55 | 400 | 771 | 117 | 1256 |
| 0·85 | 500 | 617 | 42 | 1518 |
| 1·70 | 500 | 729 | 80 | 1385 |
| 2·55 | 500 | 835 | 114 | 1314 |

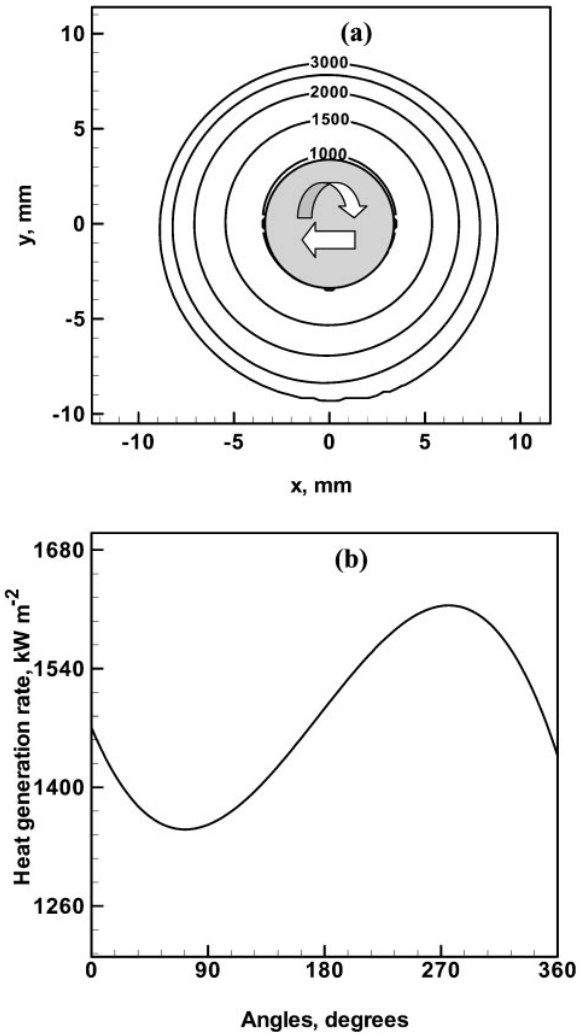


4 Spatially variable heat generation rates at *a* tool shoulder and *b* curved surface of tool pin: welding velocity was 1·693 mm $s^{-1}$ and tool rotational speed was 300 rev $min^{-1}$

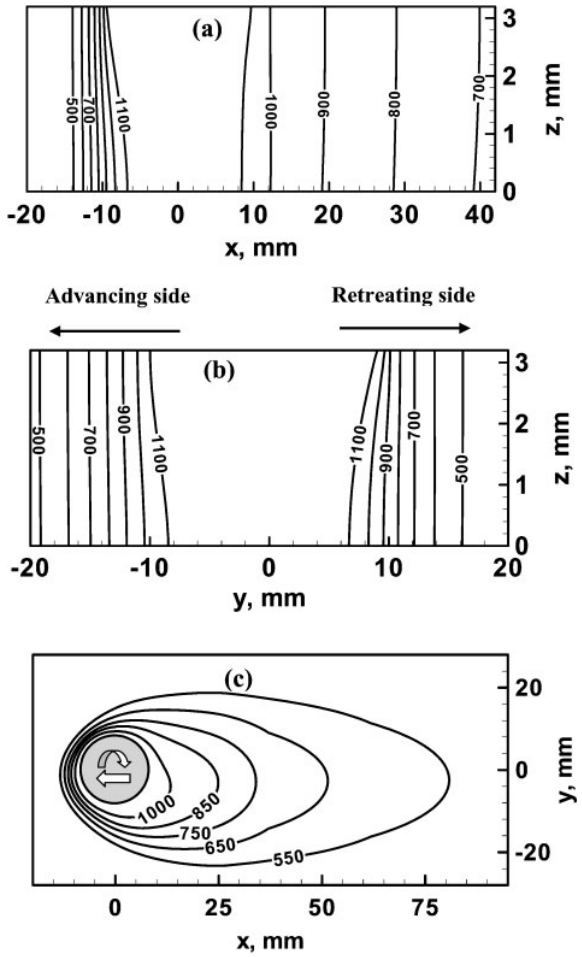


5 Computed temperature profiles (K) in *a* *y*=0 (*xz* plane), *b* *x*=0 (*yz* plane) and *c* *z*=12·7 mm (*xy* plane), i.e. top surface of workpiece: welding velocity was 1·693 mm $s^{-1}$ and tool rotational speed was 300 rev $min^{-1}$

the workpiece (Fig. 5*c*) are compressed in front of the tool and expanded behind it. The computed results are consistent with the fact that heat is supplied rapidly to the cold region of the workpiece ahead of the tool, while heat is transported at a slower rate to material already preheated behind the tool. This asymmetry results from the motion of the tool and becomes more prominent at high welding speeds. Significant asymmetry of the temperature field can also be observed from Fig. 5*b* owing to angular variation of heat generation and material flow. It may be noted that the 1100 K temperature contour on the advancing side is located at ~8·1 mm from the tool axis, while the same contour on the retreating side is placed at ~6·5 mm from the tool axis. This behaviour may be attributed to the higher heat generation rate on the advancing side because of higher relative velocity between the tool and the material. This asymmetry of local temperatures on advancing and retreating sides may also be observed from Fig. 5*c*. As expected, the temperatures are higher on the advancing side owing to higher local relative velocity between the tool and the workpiece and consequently higher local rate of heat generation.

Figure 6*a* and *b* depicts the computed thermal cycles at several monitoring locations on the advancing and retreating sides respectively. The locations are 0·98 mm below the top surface of the workpiece and at 8, 12, 16 and 22 mm away in the *y* direction from the tool axis on either the advancing or retreating side. Thermal cycles were constructed from the steady state temperature distribution by converting distance to time using welding velocity.[32] It is observed that the temperatures on the advancing side (Fig. 6*a*) are consistently higher when compared with those on the retreating side (Fig. 6*b*). This is in agreement with the observations from Fig. 5*b* and *c*. Furthermore, the results show a rapid increase in temperature during heating followed by a comparatively slower cooling as the heat source moves away from the monitoring locations. This behaviour may be further explained from the temperature contours similar to those in Fig. 5*c*. The initial rapid heating is observed as the monitoring locations encounter compressed thermal contours ahead of the tool. As the tool moves ahead of the monitoring locations, the expanded temperature contours lead to slow cooling. The higher the welding velocity, the faster the temperature changes during both heating and cooling.

The computed temperature profiles at three monitoring locations are compared with the experimental data

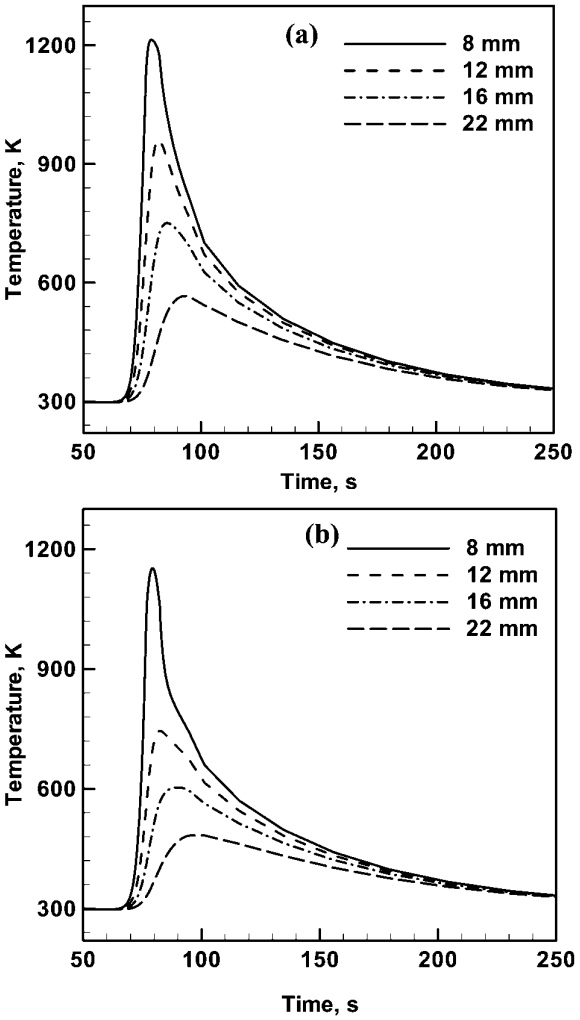


**6 Time–temperature profiles at several monitoring locations 0·98 mm below top surface and at distances of 8, 12, 16 and 22 mm from centreline perpendicular to welding direction *a* on advancing side, *b* on retreating side: welding velocity was 1·693 mm $s^{-1}$ and tool rotational speed was 300 rev $min^{-1}$**

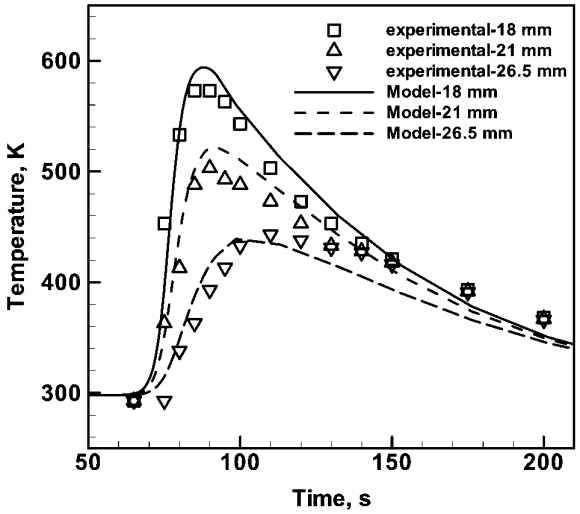


**7 Comparison between experimental[17] and calculated time–temperature profile at three monitoring locations on top surface of retreating side at distance of *y*=18, 21 and 26·5 mm: welding velocity was 1·693 mm $s^{-1}$ and rotational speed was 300 rev $min^{-1}$**

from literature[16] in Fig. 7 at $y$ distances of 18, 21 and 26·5 mm on the top surface of the retreating side. Good agreements between the experimentally determined and the computed results at different monitoring locations indicate that the model can be used to examine temperature profiles and cooling rates.

Figure 8*a* shows the variation of the computed peak temperature with welding velocity at different heat efficiency factors. The heat efficiency factor $f$ represents the fraction of heat generated at the tool/workpiece interface that is transported into the workpiece. The procedure adapted for the calculation of this factor has been adapted from literature[24,25] based on a relation explained previously in this paper in the section 'Mathematical model'. Because of the simplified nature of the heat efficiency factor expression, the sensitivity of the peak temperature on the value of the heat efficiency factor was examined. The computed results in Fig. 8*a* show that a change in the value of the heat efficiency factor from 0·4 to 0·5 leads to only $\sim$20 K change in the peak temperature. Therefore an error of $\sim$25% in the value of the heat efficiency factor would not have a significant effect on the computed peak temperature. Figure 8*a* shows that the peak temperatures varied in the 1200–1350 K range. These values are higher than those observed in the FSW of aluminium where the peak temperatures were in the 700–800 K range.[15] Figure 8*a* also indicates that the peak temperature decreases with increasing welding velocity. This behaviour originates from the fact that at high welding velocity, the heat input per unit length decreases and heat is dissipated over a large volume of the workpiece. It is also observed that the peak temperature becomes higher with higher heat efficiency factors, as expected. Figure 8*b* shows that peak temperature increases with increasing rotational velocity and heat efficiency factor. At high rotational speed, the relative velocity between the tool and workpiece is high and consequently, the heat generation rate and the temperatures are also high.

## Computed viscosity and plastic flow fields

Figure 9 shows the computed strain rate versus distance behind the tool opposite to the direction of welding at different elevations, i.e. values of $z$. It is observed that the strain rate values are $<130$ $s^{-1}$, which is similar to the values observed during FSW of aluminium.[16] It is further seen from the figure that for low values of $z$, maximum strain rate occurs near the surface of the pin where the velocity gradient is highest. At high values of $z$, i.e. near the top surface of the workpiece, the velocity gradient is high near the pin and then decreases, as for lower planes, but starts increasing a short distance away from the pin due to momentum transfer from the shoulder and is highest below the outer edge of the total shoulder where velocities are highest. It is also observed that strain rates decreases rapidly with depth, which may be attributed to large decrease in velocities through viscous dissipation.

Figure 10 shows the variation of viscosity along $x$ direction at different elevations, i.e. values of $z$. It is seen that at $z$=2·73 mm, viscosity decreases with increasing $x$ followed by a sharp increase at high values of $x$. Because

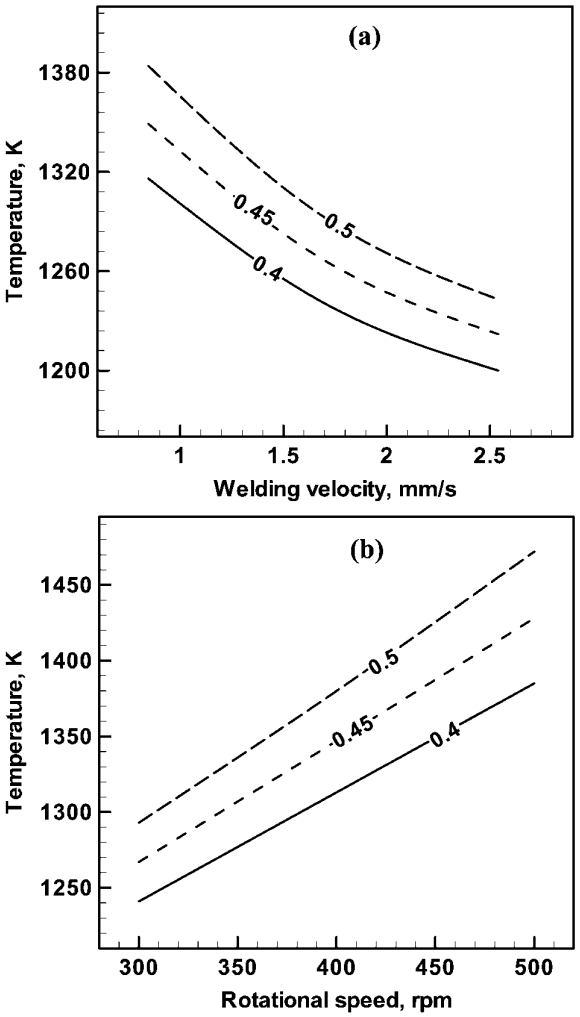


**8 Peak temperature as function of *a* welding velocity, with 300 rev min$^{-1}$ rotational speed and efficiency of heating=0·4, 0·45 and 0·5 and *b* rotational speed, with 1·693 mm s$^{-1}$ welding velocity and efficiency of heating=0·4, 0·45 and 0·5**

the viscosity is inversely proportional to local strain rate, this observation may be explained considering the values of strain rates presented in Fig. 9, where the strain rate trends are just opposite to those of the viscosity values presented in Fig. 10. At lower values of $z$, the viscosity progressively increases with $x$ distance, which is also consistent with the strain rate variations shown in Fig. 9. An important consequence of the computed viscosity profiles is that high viscosity values beyond a certain critical high value results in lack of plastic flow and define the location of the stir zone/TMAZ boundary.

Figure 11*a* and *b* shows the variation of $u$ and $v$ components of velocity at different elevations, i.e. $z$ values. It is observed that the variation and magnitude of $u$ and $v$ velocities are similar. It is also observed that the peak value of velocity is of the order of 150 mm s$^{-1}$, which is lower compared with the peak velocity typically calculated in FSW of aluminium.[16] The peak velocity is equal to the product of angular velocity, radius of the shoulder and a fraction involving the extent of slip at the interface. Therefore, because stainless steels are

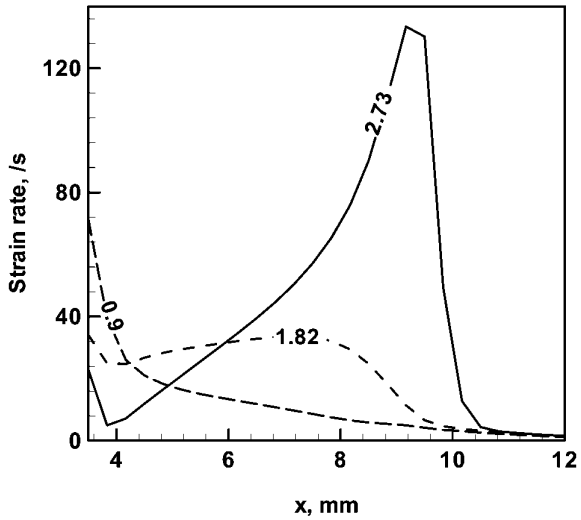


**9 Variation of strain rate as function of distance from tool pin surface opposite to welding direction at different horizontal planes at $z$=2·73, 1·82 and 0·9 mm for plate thickness of 3·18 mm: welding velocity was 1·693 mm s$^{-1}$ and the rotational speed was 300 rev min$^{-1}$**

commonly welded with smaller shoulder diameter tools[17,25] than those of aluminium alloys,[6–8] the peak velocity during the FSW of stainless steel is lower than that during FSW of aluminium alloys. It is seen from Fig. 11 that at $z$=2·73 mm, velocity increases and attains a maximum at the periphery of the shoulder, i.e. around $x$=9 mm, followed by a rapid decrease, while at planes near the bottom of the workpiece, the velocity peaks are attained at the pin surface. The velocity peaks increase and shift further away from the tool surface at higher elevations or $z$ values because of the effect of shoulder. Near the top surface, the effect of shoulder and the viscous momentum transfer is fairly pronounced resulting in high peak velocity. Because momentum

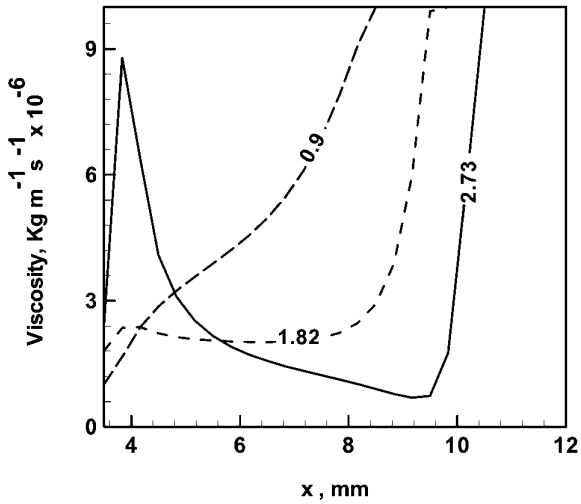


**10 Variation of viscosity as function of distance from tool pin surface opposite to welding direction, at planes corresponding to $z$=2·73, 1·82 and 0·9 mm for plate thickness of 3·18 mm: welding velocity was 1·693 mm s$^{-1}$ and rotational speed was 300 rev min$^{-1}$**

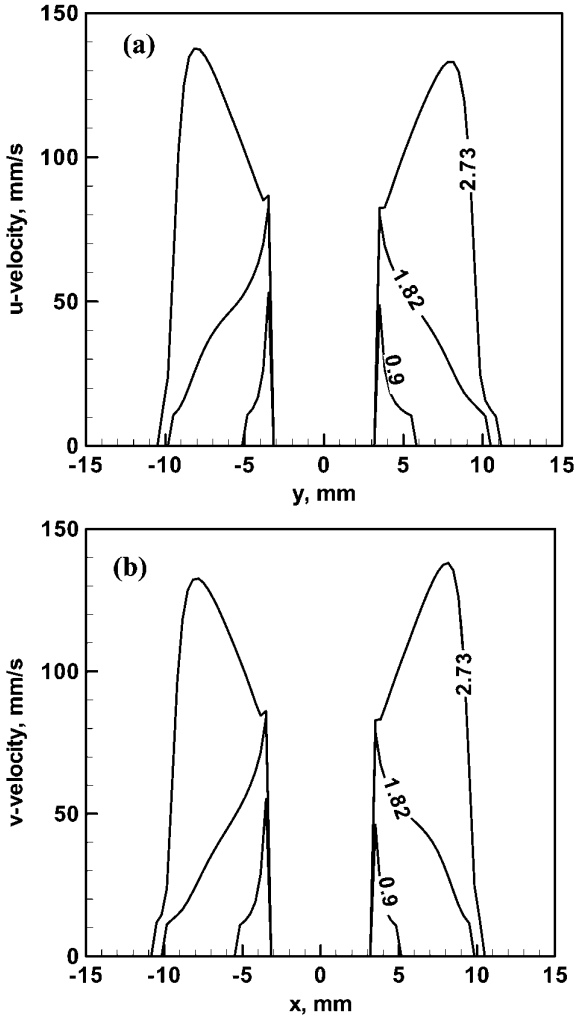


**11 Plot of variation of *a u* velocity and *b v* velocity as function of distance from tool surface for corresponding to *z*=3·72, 1·82 and 0·9 mm for 3·18 mm thick plate: welding velocity was 1·693 mm s$^{-1}$ and rotational speed was 300 rev min$^{-1}$**

decays rapidly in the $z$ direction below the shoulder, the effect of rapid rotation of the shoulder does not reach the lower elevations near the bottom of the workpiece. Figure 11 shows that the peak velocity is $\sim$150 mm s$^{-1}$ and rapidly drops beyond the periphery of the shoulder. The lower thermal conductivity of steel allows sharp decay of flow stress and velocities beyond the shoulder periphery. The momentum transfer in the vertical direction occurs entirely by viscous transport and the effect of shoulder is most pronounced in planes at mid thickness or above where the order of magnitude of velocities are $\sim$60 mm s$^{-1}$. The velocity drops gradually thereafter away from the tool pin.

The viscosity contours at different horizontal planes, i.e. $z$ values, are shown in Fig. 12. The velocity vectors are also plotted in this figure, superimposed on the viscosity contours. At the top surface near the shoulder, the $x$ and $y$ components of velocity increase with distance from the axis of the shoulder. At the same elevation, beyond the shoulder, these velocities decrease with distance from the tool axis. The distribution of the computed velocities has been explained in Fig. 11. In

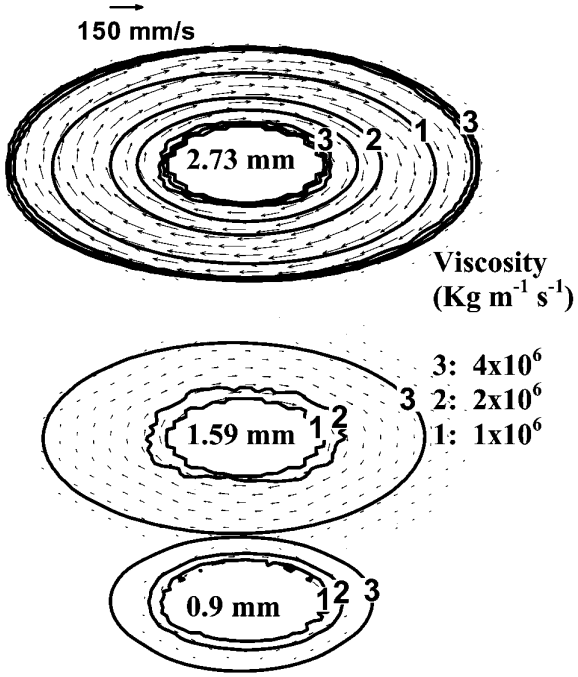


**12 Plot of spatial variation of viscosity at planes corresponding to *z*=2·73, 1·59, 0·9 mm: welding velocity was 1·693 mm s$^{-1}$ and rotational speed was 300 rev min$^{-1}$**

Fig. 12, the computed values of viscosity at the upper elevations near the shoulder show an opposite trend, i.e. a decrease followed by an increase with distance from the axis of the tool. At lower elevations away from the shoulder, the velocity decreases rapidly from the tool periphery radially outward and the viscosity profiles show an opposite trend. It may be noted that no significant material flow is observed when the viscosity is $>4\times10^6$ kg m$^{-1}$ s$^{-1}$. The region of plastic flow decreases with distance from the top surface of the workpiece. It is observed that the viscosity values fell in the $1–4\times10^6$ kg m$^{-1}$ s$^{-1}$ range. These values are of the same order as those reported for FSW of aluminium.[16] This range of non-Newtonian viscosity is consistent with the values usually observed in typical viscoplastic processing of materials such as extrusion.[35]

Figure 13 depicts the temperature contours and velocity vectors on different horizontal planes. An interesting feature to note here is that the area that contains the high plastic flow decreases with distance from the workpiece top surface. The effect of the tool shoulder as a source of momentum is most pronounced in the upper half of the workpiece. However, as only $\sim$20% of the heat is generated at the tool pin surface, and the thickness of the workpiece is much smaller than its width or length, heat is transported mainly in the vertical direction from shoulder. As a result, the high temperature region does not shrink significantly with distance from top surface. The reduction in the area where the flow occurs with distance from the shoulder produces the characteristic shape of the nugget or stir zone.

Figure 14 shows the stream trace on horizontal planes around the tool pin at three different elevations. The stream lines indicate the presence of nearly circular,

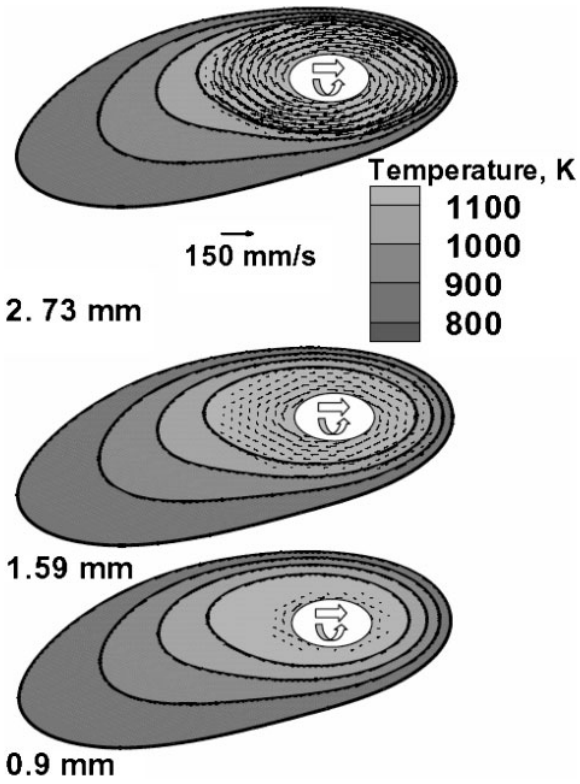


**13 Plot of temperature and velocity fields at top surface and at planes $z$=2·73, 1·59 and 0·9 mm: welding velocity was 1·693 mm s$^{-1}$ and rotational speed was 300 rev min$^{-1}$**

closed stream lines indicating recirculating flow of a plug of material, around the tool pin. These circular stream lines arise owing to the assumption of no slip condition at the tool/workpiece interface. It is further observed that these closed stream lines occupies larger areas at higher elevations, owing to higher velocities resulting from the motion of the shoulder. Beyond the region of recirculating plastic flow, the streamlines indicate that material transfer occurs mainly on the retreating side. This behaviour was also observed by Seidel and Reynolds.[9] However, the streamlines predicted by Seidel and Reynolds were more clear and circular, because they considered a 2D flow around a cylinder without any effect of a shoulder on the top. Figure 14 shows a flow reversal in the advancing side close to the pin. An important consequence of the lack of material flow on the advancing side has been related to the formation of 'wormhole' defects by Seidel and Reynolds.[9] The stagnation point is closer to the pin at lower elevations owing to a smaller region of recirculating plasticised material at these elevations.

The relative rates of heat transfer by convection and conduction is determined by the Peclet number $Pe$

$$Pe = \frac{\rho u C_p L_R}{k} \tag{24}$$

where $u$ is the velocity, $\rho$ is the density, $C_p$ is the specific heat and $L_R$ is the characteristic length. This length may be taken as the average thickness of the nugget or stir zone, which may be approximated as the distance between the tool pin surface to the shoulder periphery.

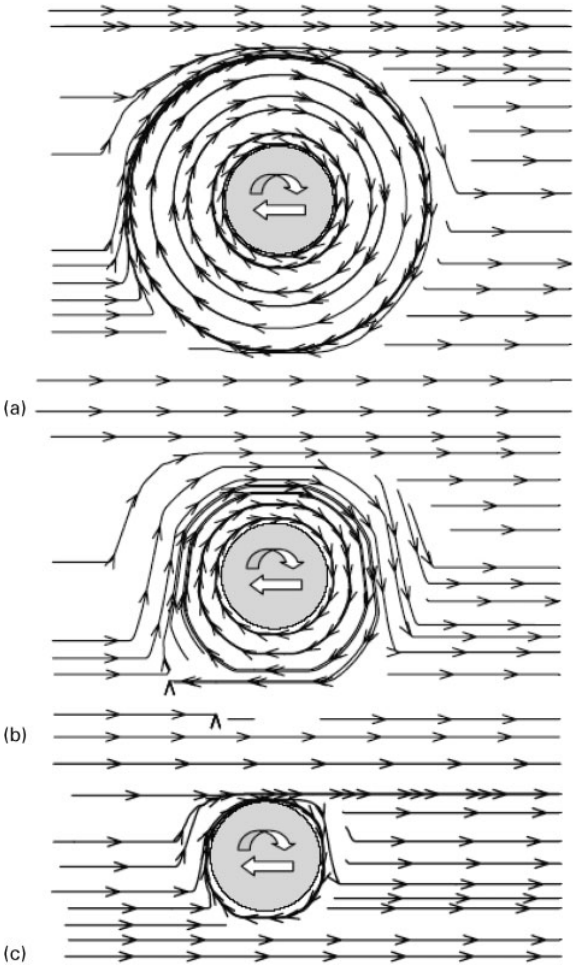


**14 Stream trace on different vertical planes at $z$=2·73, 1·59 and 0·9 mm for plate of thickness 3·18 mm: welding velocity was 4 mm s$^{-1}$ and rotational speed was 300 rev min$^{-1}$**

Taking a characteristic length of 6 mm and a characteristic velocity of 150 mm s$^{-1}$ from Fig. 12, the value of Peclet number is $\sim$170. The characteristic velocity has been taken as the peak velocity which exists near the shoulder/workpiece interface. Because the material flow is confined in a narrow region near the upper zone of the weld, Peclet number computed based on peak velocity will appropriately represent the heat transfer owing to material flow during FSW near the shoulder. This large computed value of Peclet number indicates that forced convection is very important for heat transfer during FSW of stainless steel in the high temperature region where significant plastic flow occurs. The value of $Pe$ would be much lower near the root where heat conduction would be an important mechanism of heat transfer.

## Summary and conclusions

Three dimensional temperature and plastic flow fields during friction stir welding of 304 austenitic stainless steel have been calculated by solving the equations of conservation of mass, momentum and energy. The spatially variable non-Newtonian viscosity was determined from the computed values of strain rate,

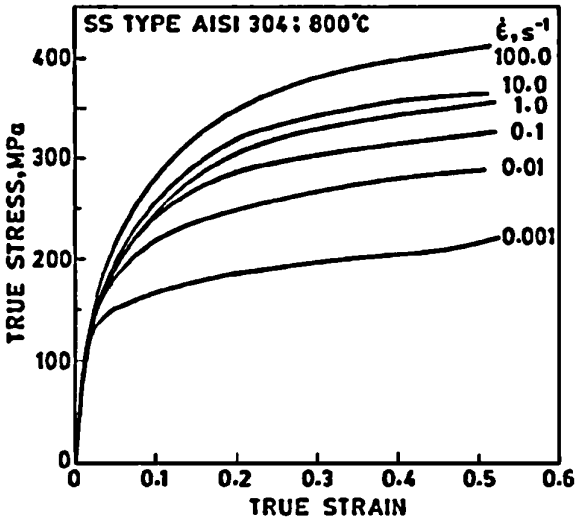


**15 Stress plotted against strain at 1073 K for 304 stainless steel at different strain rates expressed in $s^{-1}$ (Ref. 37)**

temperature and material properties. Temperature dependent thermal conductivity, specific heat and yield strength were considered. The computed results show that significant plastic flow occurs near the tool, where convective heat transfer is the main mechanism of heat transfer. The computed results show significant asymmetry of the temperature profiles around the tool because of the rotational and linear motion of the tool. The typical strain rate during FSW of stainless steel was $<130\ s^{-1}$ and viscosity ranged $1\text{–}4\times10^{6}$ kg $m^{-1}$ $s^{-1}$. The maximum value of viscosity, above which no significant material flow occurs, was found to be $4\times10^{6}$ kg $m^{-1}$ $s^{-1}$. The viscosity values were found to be of the same order as those for aluminium welding. The predicted temperature versus time plots agreed well with experimental results. The computed stream trace in the horizontal planes around the tool pin showed the presence of nearly circular closed streamlines indicating the presence of a plug of material. The region of this recirculating flow expands with elevation because of proximity to the relatively larger rotating shoulder. The stream traces also showed that most of the material flow occurred mainly on the retreating side.

## Appendix

### Strain rate and temperature dependence of yield strength

Figure 15 shows that at 1073 K, yield strength values for 304 stainless steel do not change significantly with strain rate in the strain rate range of 0·001–100 $s^{-1}$. Furthermore, yield strength has been quantified in terms of strain rate and temperature[36] in the following empirical form

$$\sigma_{ys}=\sigma_a+\sigma_p^*\exp\left[1-\frac{kT\ln(A/\dot{\varepsilon})}{\Delta H_0}\right] \quad (25)$$

where $\sigma_a$, $\sigma_p^*$, $\Delta H_0$ and $A$ are material dependent constants obtained by regression of yield strength data at different temperatures and strain rates. At high temperatures, the exponent term becomes very large and negative. As a result, the yield strength approaches a saturation value reducing strain rate sensitivity considerably. Therefore, yield strength has been assumed to be strain rate independent.

## References


1. W. M. Thomas, E. D. Nicholas, J. C. Needham, M. G. Church, P. Templesmith and C. Dawes: Int. Patent PCT/GB92/02203 and GB Patent 9125978·9, 1991.
2. M. J. Russel and H. R. Shercliff: Proc. 7th. Int. Conf. on 'Joints in aluminum', Vol. 2, 185–195; 1998, Cambridge, The Welding Institute.
3. J. E. Gould and Z. Feng: *J. Mater. Process. Manuf. Sci.*, 1998, **7**, 185–194.
4. H. Schmidt, J. Hattel and J. Wert: *Model. Simulat. Mater. Sci. Eng.*, 2004, **12**, 143–157.
5. Ø. Friggard, Ø. Grong and O. T. Midling: *Metall. Mater. Trans. A*, 2001, **32A**, 1189–1200.
6. Y. J. Chao, X. Qi and W. Tang: *ASME J. Manuf. Sci. Eng.*, 2003, **125**, 138–145.
7. M. Song and R. Kovacecic: *Proc. Inst. Mech. Eng. B.*, 2004, **218B**, 17–33.
8. M. Z. H. Khandkar, J. A. Khan and A. P. Reynolds: *Sci. Technol. Weld. Join.*, 2003, **8**, (3), 165–174.
9. T. U. Seidel and A. P. Reynolds: *Sci. Technol. Weld. Join.*, 2003, **8**, 175–183.
10. T. U. Seidel and A. P. Reynolds: *Metall. Mater. Trans. A*, 2001, **32A**, 2879–2884.
11. P. A. Colegrove and H. R. Shercliff: *Sci. Technol. Weld. Join.*, 2004, **9**, (4), 345–351.
12. P. A. Colegrove and H. R. Shercliff: *Sci. Technol. Weld. Join.*, 2004, **9**, (4), 352–361.
13. P. A. Colegrove and H. R. Shercliff: *J. Mater. Process. Technol.*, 2005, **169**, (2), 320–327.
14. C. B. Smith, G. B. Bendzsak, T. H. North, J. F. Hinrichs, J. S. Noruk and R. J. Heideman: Proc. 9th Int. Conf. on 'Computer technology in welding', Detroit, MI, USA, September 1999, 475–486. NIST, AWS, TWI.
15. P. Ulysse: *Int. J. Mach. Tool. Manuf.*, 2002, **42**, 1549–1557.
16. R. Nandan, G. G. Roy and T. DebRoy: *Metall. Mater. Trans. A*, 2006, **37A**, (4), 1247–1259.
17. X. K. Zhu and Y. J. Chao: *J. Mater. Process. Technol.*, 2004, **146**, 263–272.
18. J. H. Cho, D. E. Boyce and P. R. Dawson: *Mater. Sci. Eng. A*, 2005, **398A**, 146–163.
19. E. Hart: *J. Eng. Mater. Technol.*, 1976, **98**, 193–202.
20. W. Zhang, G. G. Roy, J. W. Elmer and T. DebRoy: *J. Appl. Phys.*, 2003, **93**, 3022–3033.
21. E. S. Fisher: *J. Nucl. Mater.*, 1966, **18**, 39–54.
22. O. C. Zienkiewicz and I. C. Cormeau: *Int. J. Numer. Method. Eng.*, 1974, **8**, 821–845.
23. X. Long and S. K. Khanna: *Sci. Technol. Weld. Join.*, 2005, **10**, (4), 482–487.
24. H. S. Carslaw and J. C. Jaeger: 'Conduction of heat in solids', 2nd edn, 87–89; 1959, Oxford, Clarendon Press.
25. T. J. Lienert, W. L. Stellwag, Jr, B. B. Grimmett and R. W. Warke: *Weld. J.*, 2003, January, 1-s–9-s.
26. S. V. Patankar: 'Numerical heat transfer and fluid flow'; 1980, New York, Hemisphere Publishing Corp.
27. A. De and T. DebRoy: *Weld. J.*, 2005, **84**, (7), 101–112.
28. S. Mishra and T. DebRoy: *J. Phys. D*, 2005, **38D**, 2977–2985.
29. W. Zhang, T. DebRoy and J. W. Elmer: *Sci. Technol. Weld. Join.*, 2005, **10**, (5), 574–582.
30. W. Zhang, T. DebRoy, T. A. Palmer and J. W. Elmer: *Acta Mater.*, 2005, **53**, (16), 4441–4453.
31. S. Mishra and T. DebRoy: *J. Appl. Phys.*, 2005, **98**, 044902.
32. X. He, T. DebRoy and P. W. Fuerschbach: *J. Appl. Phys.*, 2004, **96**, 4547–4555.
33. K. Mundra, T. DebRoy and K. M. Kelkar: *Numer. Heat Transfer*, 1996, 29, 115.
34. S. Kakac, R. K. Shah and W. Aung: 'Handbook of single phase convective heat transfer', 1·9–1·11; 1987, New York, Wiley-Interscience.
35. P. J. Halley and M. E. Mackay: *J. Rheol.*, 1994, **38**, (1), 41–51.
36. W. Lei, M. Yao and B. Chen: *Eng. Fract. Mech.*, 1996, **53**, (4), 633–643.
37. S. Venugopal, S. L. Mannan and Y. V. R. K. Prasad: *Mater. Sci. Eng. A*, 1994, **177A**, 143–149.